Topological crystalline antiferromagnetic state in tetragonal FeS

Ningning Hao,[1,2] Fawei Zheng,[3] Ping Zhang,[3,4,*] and Shun-Qing Shen[5,†]

[1]*Anhui Province Key Laboratory of Condensed Matter Physics at Extreme Conditions, High Magnetic Field Laboratory,*
Chinese Academy of Sciences, Hefei 230031, Anhui, China
[2]*Collaborative Innovation Center of Advanced Microstructures, Nanjing University, Jiangsu Province 210093, China*
[3]*Institute of Applied Physics and Computational Mathematics, Beijing 100088, China*
[4]*Beijing Computational Science Research Center, Beijing 100193, China*
[5]*Department of Physics, The University of Hong Kong, Pokfulam Road, Hong Kong, China*

Integration between magnetism and topology is an exotic phenomenon in condensed-matter physics. Here, we propose an exotic phase named topological crystalline antiferromagnetic state, in which antiferromagnetism intrinsically integrates with nontrivial topology, and we suggest such a state can be realized in tetragonal FeS. A combination of first-principles calculations and symmetry analyses shows that the topological crystalline antiferromagnetic state arises from band reconstruction induced by pair checkerboard antiferromagnetic order together with band-gap opening induced by intrinsic spin-orbit coupling in tetragonal FeS. The topological crystalline antiferromagnetic state is protected by the product of fractional translation symmetry, mirror symmetry, and time-reversal symmetry, and presents some unique features. In contrast to strong topological insulators, the topological robustness is surface dependent. These findings indicate that nontrivial topological states could emerge in pure antiferromagnetic materials, which sheds new light on potential applications of topological properties in fast-developing antiferromagnetic spintronics.

I. INTRODUCTION

Since topological insulators were discovered theoretically and experimentally [1–3], symmetry-protected topological phases have become a general principle to explore exotic quantum states of matter among complex and rich compounds [4–6]. Various combinations of time-reversal symmetry, crystal space group symmetry, and particle-hole symmetry may result in a large number of exotic topological quantum states of matter. Among these, one example is the topological crystalline insulator, in which the nontrivial topological properties are protected by point group symmetry such as rotation, reflection, mirror symmetry, etc. [7,8], and the surface boundary that preserves the underlying point group symmetry hosts the gapless surface states. To fabricate a device with topological crystalline insulators, manipulation of the spin degrees of freedom of surface electrons is essential. One possible method is to include magnetism. For example, by doping magnetic atoms to induce ferromagnetism, the quantum anomalous Hall effect can be realized in a magnetic topological insulator [9,10]. However, doping magnetic atoms in a topological state is very tough and usually requires exquisite experimental designs. If the topological states of matter possess intrinsic magnetism, there would be more room to manipulate the quantum spin of surface electrons.

In this paper, we extend the concept of topological crystalline insulators from nonmagnetic materials to antiferromagnetic materials. We demonstrate that tetragonal FeS could be in a topological crystalline antiferromagnetic state in the spirit of symmetry-protected topological phases. The nontrivial topological crystalline antiferromagnetic state is protected by a combination of fractional translation, mirror reflection, and time-reversal symmetry. The fractional translation symmetry is induced by the pair checkerboard antiferromagnetic order instead of specific lattice structure [11,12]. As a consequence, it is found that the topological crystalline antiferromagnetic state has robust gapless surface states on the crystal (010) surfaces, while on other surfaces, such as (100) and (001) surfaces, there are no robust gapless surface states due to the glide-plane mirror symmetry breaking. The existence of these surface states is dictated by a mirror Chern number [8,13]. Therefore, tetragonal FeS is an ideal candidate with integration of antiferromagnetism and topology, and provides a playground to study the intrinsic magnetic effect on the surface states of topological crystalline insulators. Furthermore, in comparison with nonmagnetic and ferromagnetic materials, the antiferromagnetic topological materials have many advantages and attract more attention [14–16]. Also, the tetragonal FeS, by itself, is a kind of unconventional superconductor at low temperatures [17]. Thus the material provides an intrinsic platform to study the interplay between topology, magnetism, and superconductivity.

II. ANTIFERROMAGNETIC ORDER

Tetragonal FeS has a simple anti-PbO structure as shown in Fig. 1(a). It has attracted great attention since the first reported superconductivity with transition temperature 4.5 K [17]. One of the important aspects of tetragonal FeS is to identify the possible magnetic-ordered state in the vicinity of superconductivity. To date, some magnetic states have been proposed for tetragonal FeS experimentally, such as the nonmagnetic metallic state, a commensurate antiferromagnetic order with wave vector $k_m = (0.25, 0.25, 0)$, the low-moment (10^{-2}–$10^{-3} \mu_B$) ferromagnetic state coexisting with superconductivity, and the high-moment (about 1 μ_B)
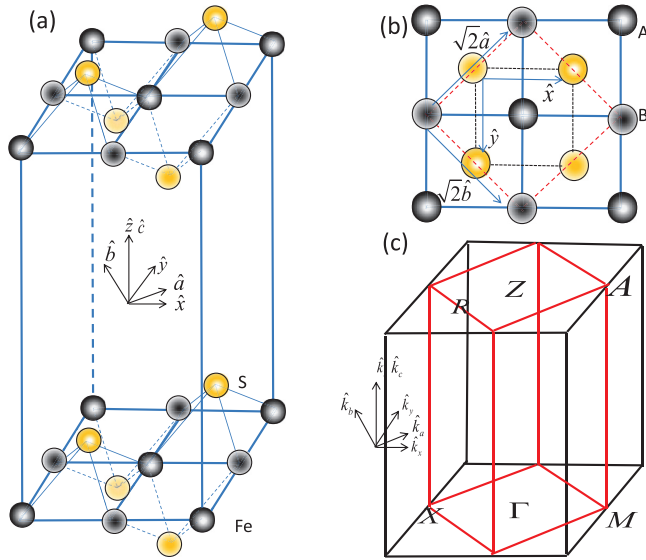
*zhang_ping@iapcm.ac.cn
†sshen@hku.hk

FIG. 1. (a) The three-dimensional (3D) view of crystal structure of tetragonal FeS. Different filling balls denote different sublattices. (b) The top-down view of tetragonal FeS with the patterns of the paramagnetic order. The black dotted and red dashed lines label the one-Fe and two-Fe unit cells. (c) Bulk Brillouin zones (BZ) of (a). Here, we take the one-Fe-unit-cell constant as length scale. $(\hat{x},\hat{y},\hat{z})$, $(\hat{a},\hat{b},\hat{c})$, $(\hat{k}_x,\hat{k}_y,\hat{k}_z)$, and $(\hat{k}_a,\hat{k}_b,\hat{k}_c)$ denote the unit direction vectors in lattice and momentum space, respectively.

ferromagnetic state coexisting with superconductivity [18–21]. These sample-dependent inconsistencies may need further efforts to be devoted into the high-quality single-crystal synthesis and relevant thin film growth.

In comparison with its widely studied isostructures such as FeSe and FeTe, first-principles calculations provide an effective method to identify the magnetic ground state of tetragonal FeS by means of determination of the lowest energy among all possible magnetic-ordered states. Possible magnetic-ordered states of tetragonal FeS include the paramagnetic order, collinear (single stripe), checkerboard (Néel), and pair checkerboard (stagger dimer) antiferromagnetic orders.

The density functional theory (DFT) and hybrid functional calculations in the present work were performed by using Vienna *ab initio* software package (VASP) [22]. The atom core electrons were described by the projector augmented wave (PAW) method [23,24]. Perdew-Burke-Ernzerhof (PBE) functional [25] was used to treat the electronic exchange correlation. The energy cutoff for the plane-wave basis was set to be 400 eV. The first Brillouin zone was sampled in the k space with a Monkhorst-Pack scheme and the grid sizes are $19 \times 19 \times 13$, $19 \times 19 \times 13$, $13 \times 13 \times 13$, and $13 \times 7 \times 13$ for PM, C-AFM, COL-AFM, and PCB-AFM phases, respectively. We have checked that the total energy is converged for the cutoff energy and the k-point sampling. The atomic structure was relaxed until the force on each atom is smaller than 0.01 eV/Å. Considering that there exists weak interlayer coupling in this composite system, we have added the van der Waals correction to the DFT calculations [26]. In order to take into account the correlation from a moderate Hubbard U interaction, the generalized gradient approximation (GGA)+U calculation method is used.

The magnetization patterns of the collinear antiferromagnetic (COL-AFM) and pair checkerboard antiferromagnetic (PCB-AFM) states are shown in Figs. 2(a), 2(b). At ambient pressure, the lattice constant of the iron plane and the S heights to the iron plane as functions of the Hubbard U are shown in Fig. 2(c). To determine the suitable Hubbard U in tetragonal FeS, we use a simple method. We start with the free lattice constants. When Hubbard U is turned on and increases from zero, the lattice sites relax freely and achieve the equilibrium positions finally. We use the obtained lattice constants to compare with the experimentally measured values. The suitable Hubbard U is read out when the two sets of lattice constants match with each other. It can be seen that the Hubbard U is reasonable to match the experimental lattice parameters with 1 eV and 0.6 eV in PCB-AFM and COL-AFM states, respectively. The COL-AFM and PCB-AFM states compete with each other as shown in Fig. 2(d). The first-principles calculations show that the COL-AFM state has a lower energy of 14 meV/Fe than the PCB-AFM state under the Hubbard U interaction correction at ambient pressure. Likewise, under ambient conditions, the recent neutron scattering experiment observed the peaks of spin excitation at wave vector $(\pi,0)$, which was the same wave vector of COL-AFM order [27]. The predictions from the first-principles calculations follow the experimental observations under ambient conditions. However, first-principles calculations predict that the PCB-AFM state becomes the lowest-energy state with increasing pressure over the threshold value of 3.5 GPa, as shown in Fig. 2(e). For instance, the energy in the PCB-AFM state is about 9 mev/Fe lower than the energy in the COL-AFM state at pressure of 4 GPa. Note that the switching between different orders tuned by pressure also occurs in bulk FeSe, in which the pressure over 2GPa can change the state of FeSe from the nematic order to long-range stable antiferromagentic order [28,29]. If the spin excitation of the PCB-AFM order was identified by neutron scattering measurement in tetragonal FeS under high-pressure conditions, it would be beneficial not only to understand the superconductivity but also to study the topological states in tetragonal FeS. Interestingly, the PCB-AFM state is predicted to be the ground state in many other iron chalcogenides such as FeSe, monolayer FeSe, and pressured FeSe [30–32].

The low-energy states with various magnetic orders in iron-based materials can be captured by a minimal Heisenberg J_1-J_2-J_3-K spin model [33],

$$H = \sum_{nn}[J_1\hat{S}_i \cdot \hat{S}_j - K(\hat{S}_i \cdot \hat{S}_j)^2]$$
$$+ \sum_{2nn} J_2\hat{S}_i \cdot \hat{S}_j + \sum_{3nn} J_3\hat{S}_i \cdot \hat{S}_j. \qquad (1)$$

Here, nn, $2nn$, and $3nn$ denote the nearest, second-nearest, and third-nearest neighbor, respectively. The mean-field phase diagram for the Hamiltonian in Eq. (1) was presented in Fig. 2 in Ref. [32]. For tetragonal FeS, the first-principles calculations give the model parameters shown in Table I. It is straightforward to check that the data in the first group give the magnetic ground state with the COL-AFM order while the data in the second group give the magnetic ground state with the PCB-AFM order, according to the phase diagram in Fig. 2(c) in Ref. [32]. Thus, we propose that the state with
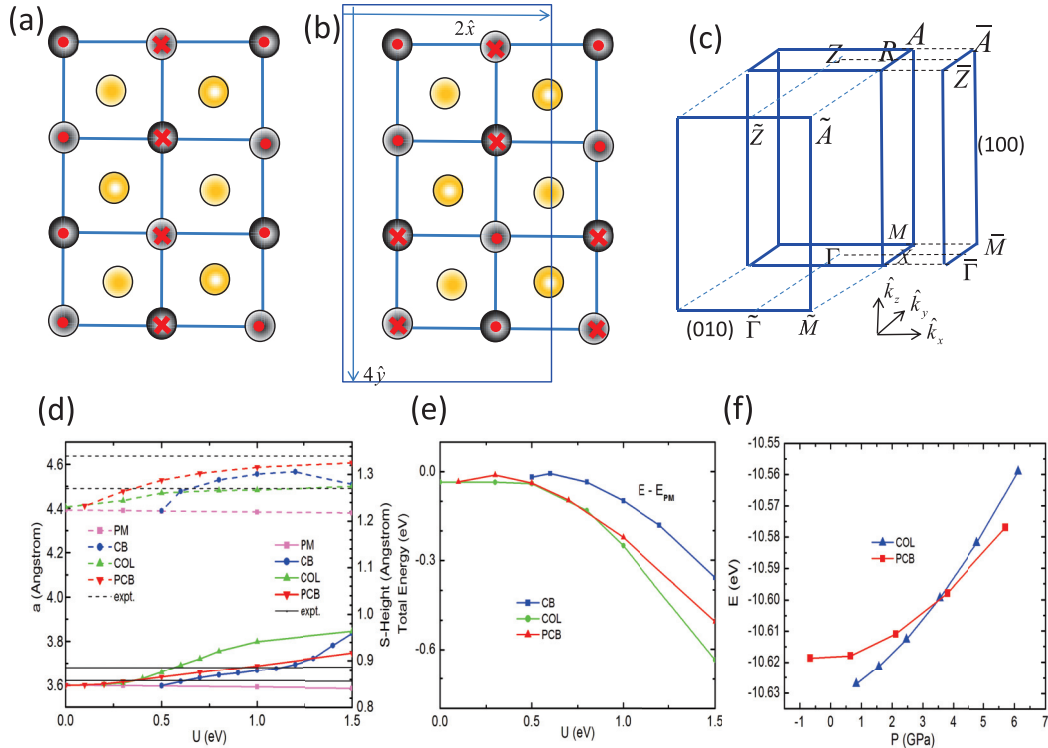
FIG. 2. (a) and (b) The top-down view of tetragonal FeS with the patterns of the COL-AFM order in (a) and the PCB-AFM order in (b). The red spots and red arrows denote the magnetization outward and inward to the iron plane. In (b) the solid blue lines label the unit cell of the PCB-AFM phase. (c) Middle: Bulk Brillouin zone of the PCB-AFM state; left: (010)-surface Brillouin zone; right: (100)-surface Brillouin zone. Here, we also take the one-Fe-unit-cell constant in the paramagnetic state as length scale. $(\hat{x}, \hat{y}, \hat{z})$, $(\hat{a}, \hat{b}, \hat{c})$, $(\hat{k}_x, \hat{k}_y, \hat{k}_z)$, and $(\hat{k}_a, \hat{k}_b, \hat{k}_c)$ denote the unit direction vectors in lattice and momentum space, respectively. (d) The in-plane lattice constants and the S atom heights to iron plane as functions of Hubbard U modulation in different magnetic phases at ambient pressure. Here, PM, C-AFM label paramagnetic and checker-board antiferromagnetic states, respectively. (e) The total energy per Fe_2S_2 relative to that in PM state as functions of Hubbard U modulation in different magnetic phases at ambient pressure. (f) The total energy E (eV) per FeS as functions of pressure P (GPa). In (d), (e), and (f), the results are from GGA+U method.

the PCB-AFM order is the magnetic ground state in tetragonal FeS at 4 GPa. As we mentioned in Sec. I, the PCB-AFM order can induce an unique topological crystalline antiferromagnetic state. In the remaining part of the paper, we focus on the discussion of how the PCB-AFM order drives the topological crystalline antiferromagnetic state and about the properties of the topological state. The properties of other antiferromagnetic states are discussed (see Ref. [34] for details).

III. BAND RECONSTRUCTION FROM PM STATE TO PCB-AFM STATE

Stable magnetic order in materials usually breaks some spatial symmetries such that the underlying electronic structures are strongly reconstructed with new features. It is widely known that the reconstructed band structures host Dirac cone structures in $BaFe_2As_2$ with the collinear AFM order [35]. The

TABLE I. The calculated parameters of tetragonal FeS for J_1-J_2-J_3-K model.

J_1	J_2	J_3	K	Pressure
127.5	84.6	-0.4	38.9	at ambient pressure
126.1	71.6	14.0	-8.2	at 4GPa

reconstructed bulk band structures for tetragonal FeS with the PCB-AFM order in the presence of spin-orbit coupling are shown in Figs. 3(a) and 3(b), which correspond to magnetization along the [100] and [001] directions, respectively. The remarkable feature in Fig. 3(a) is the emergence of Dirac points in the $k_z = 0$ and π/c planes. Slightly finite electron or hole doping can shift the Fermi level away from the Dirac points, and the Fermi surfaces form two thin tubes in three-dimensional momentum space as shown in Fig. 3(c). This means the PCB-AFM state with the [100]-direction magnetization belongs to a node-line semimetal in the undoped case even in the presence of spin-orbit coupling. Further calculations show that other PCB-AFM states with in-xy-plane magnetization, such as [010] and [110] directions, have similar results with the state with [100]-direction magnetization. However, no Dirac points survive and a fully gapped state is obtained in the PCB-AFM state with the [001]-direction magnetization in the presence of spin-orbit coupling.

To understand the band reconstruction of tetragonal FeS with the PCB-AFM order, we introduce a tight-binding model associated with mean-field approximation involving five d orbitals of Fe by ignoring p orbitals due to their negligible weight around the Fermi level shown in Fig. 3(d),

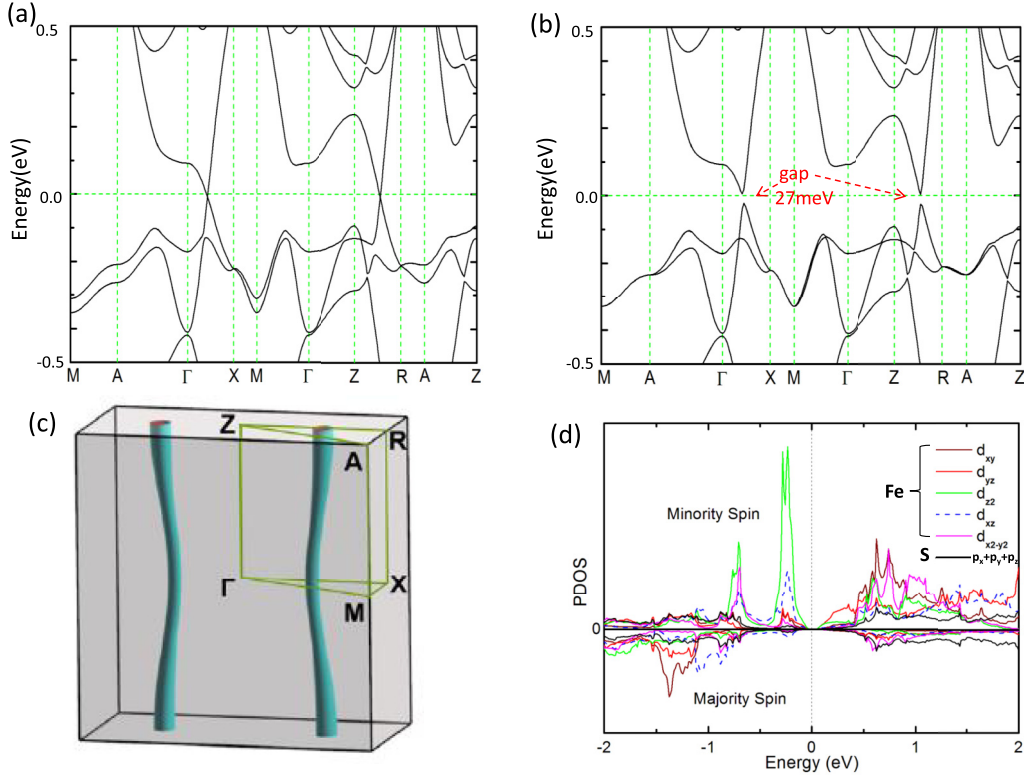$$H^{(l)} = H_0 + H^{(l)}_{\text{pcb}} + H_{so}, \qquad (2)$$

FIG. 3. (a) The band structures for the PCB-AFM state with the [100]-direction magnetization in the presence of spin-orbit coupling. (b) The band structures for the PCB-AFM state with the [001]-direction magnetization in the presence of spin-orbital coupling. (c) 3D Fermi surface corresponds to (a) when the Fermi level is slightly shifted from zero. (d) The partial density of states for d orbitals of Fe and p orbitals of S in the PCB-AFM state with the [001]-direction magnetization in the absence of spin-orbit coupling.

where

$$H_0 = \sum_{k \in BZ_{pm}} \sum_{\alpha,\beta,\sigma} \Psi^\dagger_{\alpha,\sigma}(\mathbf{k}) H_{\alpha\beta}(k) \Psi_{\beta,\sigma}(\mathbf{k}), \qquad (3)$$

$$H^{(l)}_{\text{pcb}} = \sum_{k_n \in BZ_{\text{pcb}}} \sum_{n=0,\alpha}^{3} [\Psi^\dagger_\alpha(\mathbf{k}_n) \Delta e^{-i\theta(\alpha)} s_l \Psi_\alpha(\mathbf{k}_{n+1}) + \text{H.c.}], \quad (4)$$

and

$$H_{so} = \sum_{k \in BZ_{pm}} \sum_\alpha [\Psi^\dagger_\alpha(\mathbf{k}) \lambda_{so,z} L^z s_z \Psi_\alpha(\mathbf{k})$$

$$+ \Psi^\dagger_\alpha(\mathbf{k}) \lambda_{so,\parallel}(L^x s_x + L^y s_y) \Psi_{\bar\alpha}(\mathbf{k})]. \qquad (5)$$

Here, H_0 is the tight-binding Hamiltonian describing the electronic structure in the absence of magnetic orders. $\mathbf{k} = (k_x, k_y, k_z)$ is defined in a one-Fe unit cell with $(k_x, k_y) \in [0, 2\pi]$, $k_z \in [0, 2\pi/c]$. We have transformed H_0 from the two-Fe-unit-cell representation to the one-Fe-unit-cell representation according to the parity of the glide-plane symmetric operator $\frac{1}{2}\hat{t}(\sqrt{2}\hat{a}, \sqrt{2}\hat{b}, 0)\hat{M}_z$ [36,37], with $\hat{t}$ and $\hat{M}_z$ the translation operation and mirror reflection about xy plane, respectively. α and β take o or e to label the parity of the glide-plane symmetry, and σ labels the spin degrees of freedom. $\Psi^T_{o,\sigma}(\mathbf{k}) = [d_{xy,\sigma}(\mathbf{k}+\mathbf{Q}), d_{x^2-y^2,\sigma}(\mathbf{k}+\mathbf{Q}), d_{xz,\sigma}(\mathbf{k}), d_{yz,\sigma}(\mathbf{k}), d_{z^2,\sigma}(\mathbf{k}+\mathbf{Q})]$ and $\Psi_{e,\sigma}(\mathbf{k}) = \Psi_{o,\sigma}(\mathbf{k}+\mathbf{Q})$ with $\mathbf{Q} = (\pi,\pi,0)$ denoting the folding wave vector from the one-Fe BZ to the two-Fe BZ as shown in Fig. 1(c). The exact expressions for $H_{\alpha\beta}(k)$ are presented in Ref. [34]. $H^{(l)}_{\text{pcb}}$ describes the

PCB-AFM order under the mean-field approximation. In the PCB-AFM state, one magnetic unit cell includes eight Fe atoms as shown in Fig. 2(b), and the corresponding folded wave vector is $\mathbf{Q}_1 = (\pi, \pi/2, 0)$. $\mathbf{k}_n = \mathbf{k} + n\mathbf{Q}_1$. $l = 0, x, y, z$ label the 2×2 unit matrix and Pauli matrices, respectively. $\Delta e^{-i\theta(\alpha)}$ labels the PCB-AFM order parameter with $\Delta = \text{diag}[m_{xy}, m_{x^2-y^2}, m_{xz}, m_{yz}, m_{z^2}]$ and $\theta(\alpha) = [n/2 - (-1)^\alpha]\pi$. H_{so} is the spin-orbit coupling term. $\bar\alpha$ denotes the inverse parity of α.

Figures 4(a), 4(b1)–4(b3), and 4(c) demonstrate the band reconstruction from the paramagnetic state to the PCB-AFM state. Starting from the band structure in Fig. 4(a), the wave vector $\mathbf{Q}_1$ connects electron-type band near the M (A) point with hole-type band near the Γ (Z) point, and folds one to another in the folded BZ of the PCB-AFM state as shown in Fig. 4(b1). Define the orbital energy modulations $\Delta\varepsilon_l$,

$$\Delta\varepsilon_j = e_j^{(\text{PCB})} - e_j^{(PM)}, \qquad (6)$$

where $e_j^{(\text{PCB})}$ and $e_j^{(PM)}$ denote the energy of on-site orbital indexed by j in PCB-AFM and PM states, respectively. $\Delta\varepsilon$ is induced by nematicity of the PCB-AFM state, i.e., the C_4 rotation symmetry connecting the [100] and [010] directions is broken in the PCB-AFM state. The specific values of all $\varepsilon_j^{(\text{PCB})}$ and $\varepsilon_j^{(PM)}$ are listed in Ref. [34]. When $\Delta\varepsilon_j$ is considered, only three bands are revealed to play a key role around the Fermi level as in Fig. 4(b2). After all the PCB-AFM order parameters m_j except m_{xy} are turned on, the three bands are
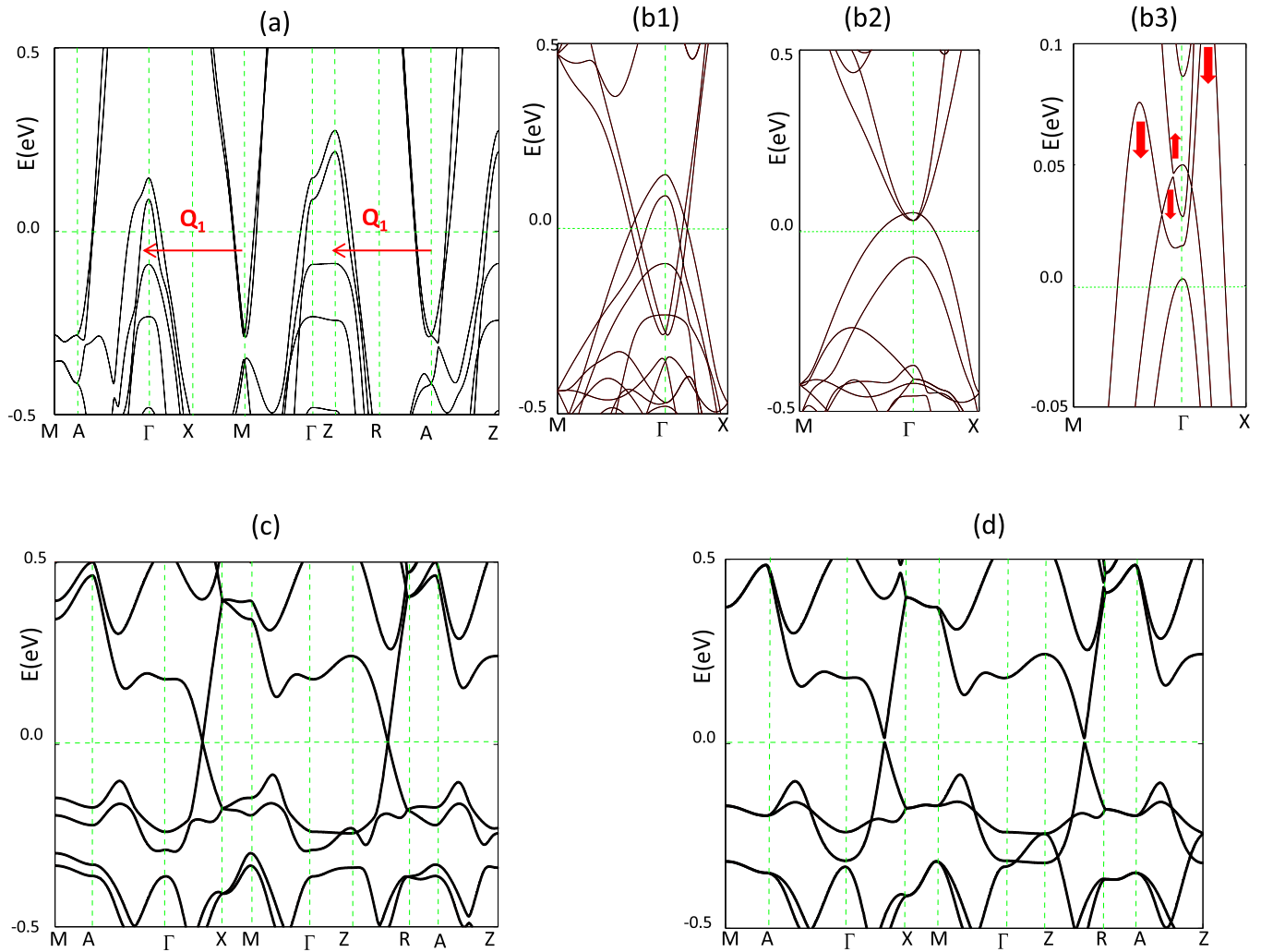
FIG. 4. (a) Band structures in the paramagnetic state in the presence of spin-orbit coupling. (b1)–(b3), (c)–(d) Bands evolution from the paramagnetic state to the PCB-AFM state along the M-Γ-X lines from the mean-field Hamiltonian in Eq. (2) for the PCB-AFM state with the [001]-direction magnetization in the presence of spin-orbit coupling. (b1) Bands of the paramagnetic state in the folded BZ of the PCB-AFM state. (b2) Turn on all $\Delta\varepsilon$ and turn off all m. (b3) Turn on all $\Delta\varepsilon$ and turn off only m_{xy}. (c) Turn on all $\Delta\varepsilon$ and all m_{xy} to obtain bands in the PCB-AFM state. We set $\lambda_{so,\parallel} = 0.03$ eV, $\lambda_{so,z} = 0.00$ eV in (c) and $\lambda_{so,\parallel} = 0.00$ eV, $\lambda_{so,z} = 0.03$ eV in (d). The modulations of the orbital energy (in units of eV) about the paramagnetic state and the PCB-AFM order parameters (in unit of μ_B) take the magnitudes as follows: $\Delta\varepsilon_{xy} = -0.375$, $\Delta\varepsilon_{x^2-y^2} = -0.075$, $\Delta\varepsilon_{xz} = -0.425$, $\Delta\varepsilon_{yz} = -0.125$, $\Delta\varepsilon_{z^2} = 0.025$; $m_{xy} = 1.04$, $m_{x^2-y^2} = 0.33$, $m_{xz} = 0.25$, $m_{yz} = 0.64$, $m_{z^2} = 0.30$. The sum of five m is about 2.5 μ_B as the result obtained from the first-principles calculations.

strongly modulated and a small band gap is opened between an electron band and a hole band along the Γ-M direction, but no band gap opens along the Γ-X direction in Fig. 4(b3). When m_{xy} increases from zero, the three bands move along the directions marked by the arrows in Fig. 4(b3). Finally, the node-line semimetal phase emerges as shown in Fig. 4(c).

Note that the band structure for the PCB-AFM state with the [001]-direction magnetization in Fig. 4(c) has nonzero spin-orbit coupling ($L^x s_x + L^y s_y$) and the band structure in Fig. 4(d) has nonzero spin-orbit coupling $L^z s_z$ with L^α and s_α ($\alpha = x, y, z$) labeling the relevant matrices under orbital and spin basis, respectively (see Ref. [34] for details). It clearly indicates that the fully gapped phase is induced by the term of $L^z s_z$. Indeed, this is the main reason for the magnetization-direction-dependent fully gapped phase. The space group is nonsymmorphic $P4/nmm$ in the paramagnetic state for the

crystal structure of tetragonal FeS shown in Fig. 1(a). The five d orbitals can be divided into two orthogonal subgroups $\{d_{xz}, d_{yz}\}$ and $\{d_{xy}, d_{x^2-y^2}, d_{z^2}\}$ according to the eigenvalues of the nonsymmorphic operator $\frac{1}{2}\hat{t}(\sqrt{2}\hat{a}, \sqrt{2}\hat{b}, 0)\hat{M}_z$. For the three t_{2g} orbitals $\{d_{xz}, d_{yz}, d_{xy}\}$, only the term of $L^z s_z$ induces coupling between two orbitals in the same subgroup $\{d_{xz}, d_{yz}\}$. Such a coupling breaks the Dirac points and results in a fully gapped state in the PCB-AFM state with the [001]-direction magnetization (nonzero $\langle s_z \rangle$). The model Hamiltonian in Eq. (2) gives an explicit description about the band reconstruction of tetragonal FeS with the PCB-AFM order.

According to the aforementioned analyses, the magnetic structures can be well described by the effective two-band model. Thus, we can construct a simple model to summarize the band reconstruction induced by the PCB-AFM order and the spin-orbit coupling. To this end, we first plot the
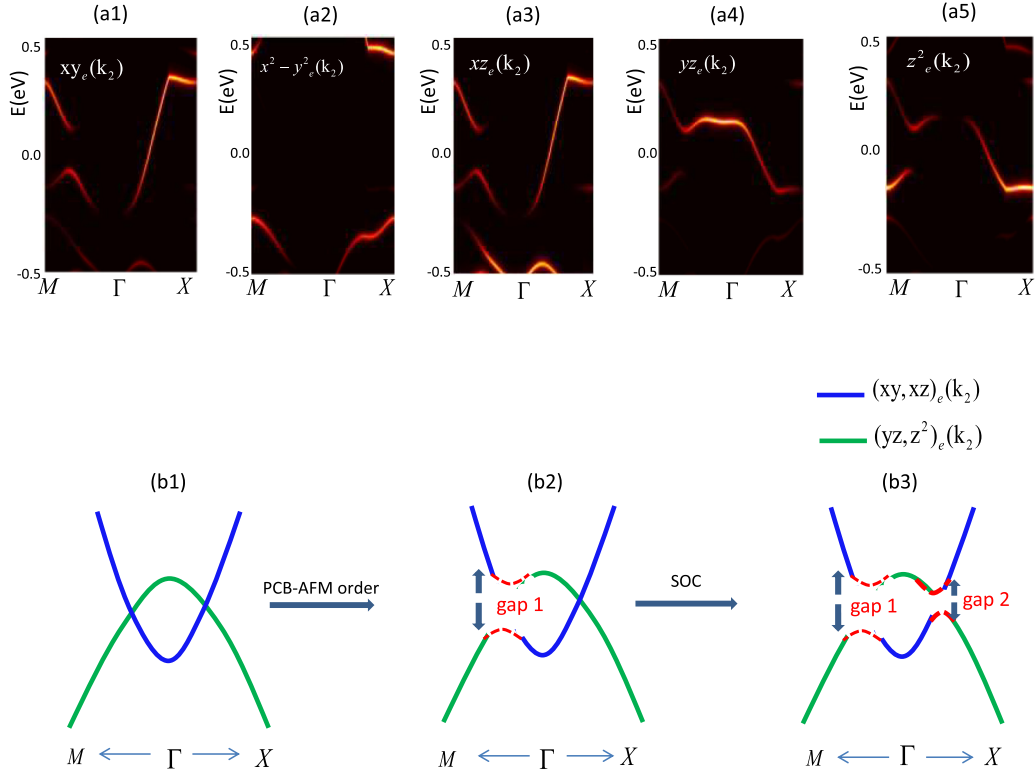
FIG. 5. (a1)–(a5) The orbital-resolved spectral function $A_e(\mathbf{k}_2,\omega)$ for five d orbitals from the mean-field Hamiltonian in Eq. (2) in the PCB-AFM state with the [001]-direction magnetization. (b1)–(b3) Under the two effective bands picture, the schematic diagrams show the topological phase transition induced by the PCB-AFM order and spin-orbit coupling in tetragonal FeS.

orbital-resolved spectral function $A_e(\mathbf{k}_2,\omega)$ of the PCB-AFM state with the [001]-direction magnetization in the absence of the spin-orbit coupling in Figs. 5(a1)–5(a5). It clearly shows that the four d orbitals of iron can be divided into two groups to form two sets of the effective bands shown in Fig. 5(b1). Note that the band inversion condition is natural due to the folding induced by the PCB-AFM wave vector $\mathbf{Q}_1$ through comparing Fig. 5(b1) with Figs. 4(a), 4(b1). After the PCB-AFM order is turned on, the two bands couple with each other and open a gap along the Γ-M direction but not along the Γ-X direction as shown in Fig. 5(b2). Finally, the Dirac node is fully gapped along the Γ-X direction, because the spin-orbit coupling only concurs with the magnetization along the [001] direction as shown in Fig. 5(b3).

IV. TOPOLOGICAL ROBUST SURFACE STATES AND TOPOLOGICAL INVARIANTS

To assess the topological characteristics of the gapped band structure of tetragonal FeS shown in Fig. 3(b), the spectra of surface states is directly computed. The PCB-AFM order shown in Fig. 2(b) corresponds to a wave vector $(\pi,\pi/2,0)$, thus the surface commensurate with the PCB-AFM order includes (100) and (010) surfaces. Using the first-principles calculations, we explicitly demonstrate the presence of the surface states in a slab geometry in Figs. 6(a) and 6(b) for (010) and (100) S-terminated surface cuts, respectively. The results for the Fe-terminated surface cuts are similar. We extract the localized surface bands and plot the topologically equivalent

schematic diagrams in Figs. 6(c) and 6(d) to show the key features of the surface states. One can find that the localized (010) surface bands cross the band gap, which implies the nontrivial properties as shown in Figs. 6(c) and 6(e), while the two middle localized surface bands of the (100) surface open a gap and do not cross the band gap as shown in Figs. 6(d) and 6(f). The surface spectra definitely demonstrate the tetragonal FeS with the PCB-AFM order hosts a surface-dependent nontrivial topological phase.

In the spirit of the principles of symmetry-protected topological phases, the topological robustness of the surface states is protected by symmetries. To elucidate the characteristics of the surface states, we first need to analyze the symmetries owned by (010) and (100) surfaces. Given the PCB-AFM pattern shown in Fig. 2(b) with the [001]-direction magnetization and taking the midpoint of the Fe-Fe bond as origin, the (010) surface has the glide-plane mirror symmetry $\frac{1}{2}\hat{t}(2\hat{x},0,0)\hat{M}_z$, and the glide-plane time-reversal symmetry $\frac{1}{2}\hat{t}(2\hat{x},0,0)\hat{T}$ with $\hat{T}$ the time-reversal operator; the (100) surface has only glide-plane time-reversal symmetry $\frac{1}{2}\hat{t}(0,4\hat{y},0)\hat{T}$. Note that the fractional translation must be combined with the point group operators and time-reversal operator to guarantee system invariant under the combined operations in the presence of antiferromagnetic order [38,39]. The surface states can be classified according to the eigenvalues of the relevant symmetry. The representations of symmetry operators upon the surface states can be constructed as follows: $\frac{1}{2}\hat{t}(2\hat{x},0,0)\hat{M}_z = -ie^{-ik_x}s_z$, $\hat{M}_x = -is_x$, $\frac{1}{2}\hat{t}(2\hat{x},0,0)\hat{T} = -ie^{-ik_x}s_y\mathcal{K}$, and $\frac{1}{2}\hat{t}(0,4\hat{y},0)\hat{T} = -ie^{-i2k_y}s_y\mathcal{K}$ with $\mathcal{K}$ the complex conjugate operator.
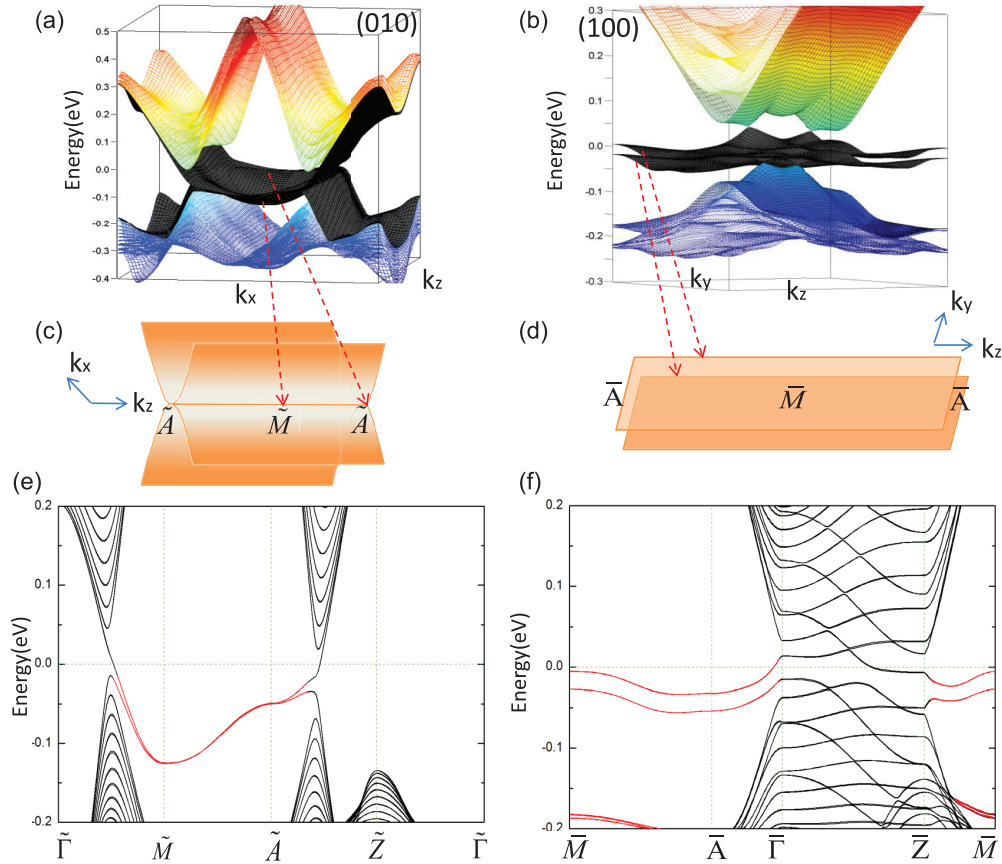
FIG. 6. (a) The band structures for the PCB-AFM state with the [001]-direction magnetization in the presence of spin-orbit coupling with surface cuts about the [010] directions. The thickness of the slab is 20 iron layers. (b) The band structures for the PCB-AFM state with the [001]-direction magnetization in the presence of spin-orbit coupling with surface cuts about the [100] directions. The thickness of the slab is 16 iron layers. In (a) and (b), the middle heavy black colored bands are localized surface bands. (c) and (d) are schematic diagrams of the localized surface bands, which are topologically equivalent to the localized surface bands in (a) and (b), respectively. (e) and (f) are the surface bands along the high-symmetry lines in surface BZ shown in Fig. 2(c), and the localized surface bands are labeled with red color. (e) and (f) correspond to (a) and (b), respectively. The thickness of the slab is 60 iron layers in (e) and 40 iron layers in (f).

For details, we first discuss the (010) surface. (i) Along the $\tilde{M}$-$\tilde{A}$ line, the surface bands are a doublet protected by a product operator $\frac{1}{2}\hat{t}(2\hat{x},0,0)\hat{T}\hat{M}_z$, which results in the pseudo-Kramers degeneracy shown in Fig. 6(e) through the antiunitary property $[\frac{1}{2}\hat{t}(2\hat{x},0,0)\hat{T}\hat{M}_z]^2 = e^{-i2k_x}|_{k_x=\pi/2} = -I$. (ii) Along both $\tilde{\Gamma}$-$\tilde{M}$ ($k_z = 0$) and $\tilde{Z}$-$\tilde{A}$ ($k_z = \pi/c$) lines, $[\frac{1}{2}\hat{t}(2\hat{x},0,0)\hat{M}_z]^2 = -e^{-i2k_x}I$ means two branches for mirror eigenvalues $\pm ie^{-ik_x}$. The time-reversal symmetry enforces the $\frac{1}{2}\hat{t}(2\hat{x},0,0)\hat{M}_z$ eigenvalues to be paired as $\{+i,-i\}$ at $k_x = 0$ and $\{1,-1\}$ at $k_x = \pi/2$. However, the degenerate points at $\tilde{\Gamma}$ or $\tilde{Z}$ labeled by $\{+i,-i\}$ merge into the bulk bands and no edge states survive along the $\tilde{\Gamma}$-$\tilde{Z}$ line as shown in Fig. 6(e). Fortunately, the degeneracy at the $\tilde{M}$ and $\tilde{A}$ points labeled by mirror eigenvalues $\{1,-1\}$ indicates the nontrivial topological properties of the (010) surface states as shown in Fig. 6(e). Note that the degeneracy between the $\tilde{M}$ and $\tilde{A}$ can be slightly gapped by artificially adding the symmetry-allowed high-order terms without breaking the degeneracy at the $\tilde{M}$ and $\tilde{A}$ points. As such, the node line connecting the $\tilde{M}$ and $\tilde{A}$ is reduced into two Dirac nodes at the $\tilde{M}$ and $\tilde{A}$ points, and the topological nature of the (010) surface is characterized by a

mirror Chern number $n_M = (n_1 - n_{-1})/2 = 2$ [8,13]. However, the symmetry-allowed high-order terms are negligibly small from the first-principles calculations, because such terms result from the interlayer couplings along the [001] direction and are beyond the nearest-neighbor coupling. The constraints from (i) and (ii) determine the characteristics of the (010) surface states. For the (100) surface, along the $\bar{M}$-$\bar{A}$ line, the product operator has the property of $[\frac{1}{2}\hat{t}(0,4\hat{y},0)\hat{T}]^2 = -e^{-i4k_y}|_{k_y=\pi/4}I = I$. Thus, the in-gap surface states are not degenerate as shown in Fig. 6(f). Along the $\bar{\Gamma}$-$\bar{Z}$ line, the surface bands merge into the bulk bands as shown in Figs. 6(b) and 6(f). The remarkable difference between the (010) and (100) surfaces roots in the strong nematicity accompanying the PCB-AFM order, which respects the glide-plane mirror symmetry $\frac{1}{2}\hat{t}(2\hat{x},0,0)\hat{M}_z$ of the (010) surface, but breaks the glide-plane mirror symmetry $\frac{1}{2}\hat{t}(0,4\hat{y},0)\hat{M}_z$ of the (100) surface. Further combination between the glide-plane mirror symmetry $\frac{1}{2}\hat{t}(2\hat{x},0,0)\hat{M}_z$ and time-reversal symmetry gives the product symmetry $\frac{1}{2}\hat{t}(2\hat{x},0,0)\hat{T}\hat{M}_z$, which protects the topological crystalline antiferromagnetic state here.

V. DISCUSSION

The nontrivial surface states hosted by tetragonal FeS are determined by the orientation of magnetization of PCB-AFM order. For a tetragonal crystal, the spontaneous easy axis or easy plane of the magnetization is determined by the intrinsic uniaxial anisotropy and tetragonal anisotropy from the crystallographic structure. Our first-principles calculations show that the energy difference between the case with the [001]-direction magnetization and the case with in-xy-plane magnetization is about 0.25 meV/Fe, which is very small. Recent spin-resolved STM measurement has shown that the magnetization tends to be out-of-xy-plane direction near the surface of bulk $Fe_{1+y}Te$ [40]. This indicates that some secondary external effects, such as pressure, mechanical stress, and alloying, can play an important role in tuning the easy axis of magnetization. Indeed, mechanical stress is widely applied in the study of antiferromagnetic states in iron-based superconductors [41,42]. The strain effect is the inverse of magnetostriction, and the energy density associated with the strain can be written as $\mathcal{E} = -\frac{3}{2}\lambda\sigma\cos^2\theta$, where σ is the stress, λ is the magnetostriction constant, and the angle θ measures the direction of the magnetization relative to the direction of the uniform stress. For a positive λ, the easy axis is the [001] direction when the stress is along the [001] direction. Thus, modulation of the direction of magnetization supplies a new method to control the charge and quantum transport of the surface electrons.

One of the remarkable features of tetragonal FeS is the presence of superconductivity at low temperatures. A consubstantial structure, in which one side is an superconducting sample and the other side is an topological crystalline antiferromagnetic state sample, can be fabricated to study the superconducting proximity effect, leading to topological superconductivity. In comparison with a heterostructure fabricated by conventional superconductors and topological insulators or semiconductors [43,44], such a consubstantial structure has many advantages to eliminate the complexity and unpredictability induced by the mismatched interface couplings from different materials, and may provide a platform to explore new physics resulting from the interplay of topology, magnetism, and superconductivity.

In conclusion, a topological crystalline antiferromagnetic state is proposed to be present accompanying the PCB-AFM state of tetragonal FeS, which is protected by the triple fractional translation, mirror reflection, and time-reversal symmetry. The finding sheds light on exploring new topological phases protected by nonsymmorphic symmetry in antiferromagnetic materials.

[1] M. Z. Hasan and C. L. Kane, Colloquium: Topological insulators, Rev. Mod. Phys. **82**, 3045 (2010).

[2] X.-L. Qi and S.-C. Zhang, Topological insulators and superconductors, Rev. Mod. Phys. **83**, 1057 (2011).

[3] S. Q. Shen, *Topological Insulators: Dirac Equation in Condensed Matters* (Springer, Berlin, 2012).

[4] A. P. Schnyder, S. Ryu, A. Furusaki, and A. W. W. Ludwig, Classification of topological insulators and superconductors in three spatial dimensions, Phys. Rev. B **78**, 195125 (2008).

[5] X. Chen, Z.-C. Gu, Z.-X. Liu, and X.-G. Wen, Symmetry-protected topological orders in interacting bosonic systems, Science **338**, 1604 (2012).

[6] Z.-C. Gu and X.-G. Wen, Tensor-entanglement-filtering renormalization approach and symmetry-protected topological order, Phys. Rev. B **80**, 155131 (2009).

[7] L. Fu, Topological Crystalline Insulators, Phys. Rev. Lett. **106**, 106802 (2011).

[8] T. H. Hsieh, H. Lin, J. Liu, W. Duan, A. Bansil, and L. Fu, Topological crystalline insulators in the SnTe material class, Nat. Commun. **3**, 982 (2012).

[9] R. Yu, W. Zhang, H. J. Zhang, S. C. Zhang, X. Dai, and Z. Fang, Quantized anomalous Hall effect in magnetic topological insulators, Science **329**, 61 (2010).

[10] C.-Z. Chang, J. Zhang, X. Feng, J. Shen, Z. Zhang, M. Guo, K. Li, Y. Ou, P. Wei, L.-L. Wang, Z.-Q. Ji, Y. Feng, S. Ji, X. Chen, J. Jia, X. Dai, Z. Fang, S.-C. Zhang, K. He, Y. Wang, L. Lu, X.-C. Ma, and Q.-K. Xue, Experimental observation of the quantum anomalous Hall effect in a magnetic topological insulator, Science **340**, 167 (2013).

[11] Z. Wang, A. Alexandradinata, R. J. Cava, and B. A. Bernevig, Hourglass fermions, Nature (London) **532**, 189 (2016).

[12] P.-Y. Chang, O. Erten, and P. Coleman, Topological Möbius Kondo in sulators, Nat. Phys. **13**, 794 (2017).

[13] J. C. Y. Teo, L. Fu, and C. L. Kane, Surface states and topological invariants in three-dimensional topological insulators: Application to $Bi_{1-x}Sb_x$, Phys. Rev. B **78**, 045426 (2008).

[14] J. Barker and O. A. Tretiakov, Static and Dynamical Properties of Antiferromagnetic Skyrmions in the Presence of Applied Current and Temperature, Phys. Rev. Lett. **116**, 147203 (2016).

[15] X. Zhang, Y. Zhou, and M. Ezawa, Antiferromagnetic skyrmion: Stability, creation and manipulation, Sci. Rep. **6**, 24795 (2016).

[16] T. Jungwirth, X. Marti, P. Wadley, and J. Wunderlich, Antiferromagnetic spintronics, Nat. Nano. **11**, 231 (2016).

[17] X. Lai, H. Zhang, Y. Wang, X. Wang, X. Zhang, J. Lin, and F. Huang, Observation of superconductivity in tetragonal FeS, J. Am. Chem. Soc. **137**, 10148 (2015).

[18] C. K. H. Borg, X. Zhou, C. Eckberg, D. J. Campbell, S. R. Saha, J. Paglione, and E. E. Rodriguez, Strong anisotropy in nearly ideal tetrahedral superconducting FeS single crystals, Phys. Rev. B **93**, 094522 (2016).

[19] S. J. Kuhn, M. K. Kidder, W. M. Chance, C. dela Cruz, M. A. McGuire, D. S. Parker, L. Li, L. Debeer-Schmitt, J. Ermentrout, K. Littrell, M. R. Eskildsen, and A. S. Sefat, FeS: Structure and composition relations to superconductivity and magnetism, Physica C **534**, 29 (2017).

[20] S. Holenstein, U. Pachmayr, Z. Guguchia, S. Kamusella, R. Khasanov, A. Amato, C. Baines, H.-H. Klauss, E. Morenzoni, D. Johrendt, and H. Luetkens, Coexistence of low-moment magnetism and superconductivity in tetragonal FeS and suppression of T_c under pressure, Phys. Rev. B **93**, 140506 (2016).

[21] F. K. K. Kirschner, F. Lang, C. V. Topping, P. J. Baker, F. L. Pratt, S. E. Wright, D. N. Woodruff, S. J. Clarke, and S. J. Blundell, Robustness of superconductivity to competing magnetic phases in tetragonal FeS, Phys. Rev. B **94**, 134509 (2016).

[22] G. Kresse and J. Furthmüller, Efficient iterative schemes for *ab initio* total-energy calculations using a plane-wave basis set, Phys. Rev. B **54**, 11169 (1996).

[23] P. E. Blöchl, Projector augmented-wave method, Phys. Rev. B **50**, 17953 (1994).

[24] G. Kresse and D. Joubert, From ultrasoft pseudopotentials to the projector augmented-wave method, Phys. Rev. B **59**, 1758 (1999).

[25] J. P. Perdew, K. Burke, and M. Ernzerhof, Generalized Gradient Approximation Made Simple, Phys. Rev. Lett. **77**, 3865 (1996).

[26] J. Klimeš, D. R. Bowler, and A. Michaelides, Van der Waals density functionals applied to solids, Phys. Rev. B **83**, 195131 (2011).

[27] H. Man, J. Guo, R. Zhang, R. U. Schonemann, Z. Yin, M. Fu, M. B. Stone, Q. Huang, Y. Song, W. Wang, D. Singh, F. Lochner, T. Hickel, I. Eremin, L. Harriger, J. W. Lynn, C. Broholm, L. Balicas, Q. Si, and P. Dai, Spin excitations and the Fermi surface of superconducting FeS, New J. Phys. **2**, 14 (2017).

[28] J. P. Sun, K. Matsuura, G. Z. Ye, Y. Mizukami, M. Shimozawa, K. Matsubayashi, M. Yamashita, T. Watashige, S. Kasahara, Y. Matsuda, J.-Q. Yan, B. C. Sales, Y. Uwatoko, J.-G. Cheng, and T. Shibauchi, Dome-shaped magnetic order competing with high-temperature superconductivity at high pressures in FeSe, Nat. Commn. **7**, 12146 (2016).

[29] J. P. Sun, G. Z. Ye, P. Shahi, J.-Q. Yan, K. Matsuura, H. Kontani, G. M. Zhang, Q. Zhou, B. C. Sales, T. Shibauchi, Y. Uwatoko, D. J. Singh, and J.-G. Cheng, High-T_c Superconductivity in FeSe at High Pressure: Dominant Hole Carriers and Enhanced Spin Fluctuations, Phys. Rev. Lett. **118**, 147004 (2017).

[30] H.-Y. Cao, S. Chen, H. Xiang, and X.-G. Gong, Antiferromagnetic ground state with pair-checkerboard order in FeSe, Phys. Rev. B **91**, 020504(R) (2015).

[31] K. Liu, Z.-Y. Lu, and T. Xiang, Nematic antiferromagnetic states in bulk FeSe, Phys. Rev. B **93**, 205154 (2016).

[32] J. K. Glasbrenner, I. I. Mazin, H. O. Jeschke, P. J. Hirschfeld, R. M. Fernandes, and R. Valentí, Effect of magnetic frustration on nematicity and superconductivity in iron chalcogenides, Nat. Phys. **11**, 953 (2015).

[33] J. Hu, B. Xu, W. Liu, N.-N. Hao, and Y. Wang, Unified minimum effective model of magnetic properties of iron-based superconductors, Phys. Rev. B **85**, 144403 (2012).

[34] See Supplemental Material at http://link.aps.org/supplemental/10.1103/PhysRevB.96.165102 for the properties of other antiferromagnetic states, detailed forms of tigh-binding model, and spin-orbit coupling.

[35] P. Richard, K. Nakayama, T. Sato, M. Neupane, Y.-M. Xu, J. H. Bowen, G. F. Chen, J. L. Luo, N. L. Wang, X. Dai, Z. Fang, H. Ding, and T. Takahashi, Observation of Dirac Cone Electronic Dispersion in BaFe₂As₂, Phys. Rev. Lett. **104**, 137001 (2010).

[36] N. Hao and J. Hu, Topological Phases in the Single-Layer FeSe, Phys. Rev. X **4**, 031053 (2014).

[37] N. Hao and S.-Q. Shen, Topological superconducting states in monolayer FeSe/SrTiO₃, Phys. Rev. B **92**, 165104 (2015).

[38] R. S. K. Mong, A. M. Essin, and J. E. Moore, Antiferromagnetic topological insulators, Phys. Rev. B **81**, 245209 (2010).

[39] C. Fang, M. J. Gilbert, and B. A. Bernevig, Topological insulators with commensurate antiferromagnetism, Phys. Rev. B **88**, 085406 (2013).

[40] T. Hänke, U. R. Singh, L. Cornils, S. Manna, A. Kamlapure, M. Bremholm, E. M. J. Hedegaard, B. B. Iversen, P. Hofmann, J. Hu, Z. Mao, J. Wiebe, and R. Wiesendanger, Reorientation of the diagonal double-stripe spin structure at Fe₁₊ᵧTe bulk and thin-film surfaces, Nat. Comms. **8**, 13939 (2016).

[41] J.-H. Chu, J. G. Analytis, K. D. Greve, P. L. McMahon, Z. Islam, Y. Yamamoto, and I. R. Fisher, In-plane resistivity anisotropy in an underdoped iron arsenide superconductor, Science **329**, 824 (2010).

[42] M. A. Tanatar, E. C. Blomberg, A. Kreyssig, M. G. Kim, N. Ni, A. Thaler, S. L. Bud'ko, P. C. Canfield, A. I. Goldman, I. I. Mazin, and R. Prozorov, Uniaxial-strain mechanical detwinning of CaFe₂As₂ and BaFe₂As₂ crystals: Optical and transport study, Phys. Rev. B **81**, 184508 (2010).

[43] L. Fu and C. L. Kane, Superconducting Proximity Effect and Majorana Fermions at the Surface of a Topological Insulator, Phys. Rev. Lett. **100**, 096407 (2008).

[44] R. M. Lutchyn, J. D. Sau, and S. D. Sarma, Majorana Fermions and a Topological Phase Transition in Semiconductor-Superconductor Heterostructures, Phys. Rev. Lett. **105**, 077001 (2010).